J Sol-Gel Sci Technol (2008) 48:239–252
DOI 10.1007/s10971-008-1816-y

ORIGINAL PAPER

Investigation of the amorphous to crystalline phase transition of chemical solution deposited $Pb(Zr_{0.3}Ti_{0.7})O_3$ thin films by soft X-ray absorption and soft X-ray emission spectroscopy

T. Schneller · H. Kohlstedt · A. Petraru · R. Waser · J. Guo · J. Denlinger · T. Learmonth · Per-Anders Glans · K. E. Smith

Received: 31 March 2008 / Accepted: 24 July 2008 / Published online: 10 September 2008

Abstract Chemical solution deposited (CSD) complex oxide thin films attract considerable interest in various emerging fields as for example, fuel cells, ferroelectric random access memories or coated conductors. In the present paper the results of soft-X-ray spectroscopy between 280 and 560 eV on the amorphous to crystalline phase transition of ferroelectric $Pb(Zr_{0.3}Ti_{0.7})O_3$ (PZT) thin films are presented. Five CSD samples derived from the same wafer coated with a PZT film pyrolyzed at 350 °C were heat treated at different temperatures between 400 and 700 °C. At first the samples were morphologically and electrically characterized. Subsequently the soft-X-ray absorption and emission experiments were performed at the undulator beamline 8.0 of the Advanced Light Source of the Lawrence Berkeley National Laboratory. Soft-X-ray absorption spectra were acquired for the Ti $L_{2,3}$-, O K-, and C K-edge thresholds by using simultaneously the total electron yield (TEY) and total fluorescence yield (TFY) detection methods. For two samples, annealed at 400 and 700 °C, respectively, the resonant inelastic soft-X-ray spectroscopy (RIXS) was applied for various excitation energies near the Ti L-, O K-edges. We observed clear evidence of a rutile phase at untypically low temperatures. This rutile phase transforms into the perovskite phase upon increasing annealing temperature. These results are discussed in the framework of current microscopic models of the PZT (111) texture selection.

Keywords Chemical solution deposition · Complex oxide films · Ferroelectric · PZT · Thin films · XRD · XAS · RIXS · Microstructure · Hysteresis

1 Introduction

Solid solutions of lead titanate and various amounts of lead zirconate, $Pb(Zr_{1-x}Ti_x)O_3$ (PZT), in form of thin films find extensive applications in non-volatile ferroelectric random access memories (FeRAMs), actuators in micro-electronic mechanical systems (MEMS), as well as infrared sensors [1–5], due to their exceptional ferroelectric, pyroelectric, and piezoelectric properties.

Numerous thin film deposition techniques such as molecular beam epitaxy, sputtering, and pulsed laser deposition are currently under development to grow high quality PZT films [6, 7]. Beside these physically based methods, chemically related techniques attracted considerable interest. While metal-organic chemical vapor deposition (MOCVD) is a key technique for conformal coverage of narrow 3-dimensional electrode structures [8–10], chemical solution deposition (CSD) [11] is a comparatively inexpensive and highly flexible technique which is applied for planar FeRAM cells, actuators and sensors [12]. In particular CSD offers the specific

T. Schneller
Institute of Materials for Electronic Engineering 2, RWTH-Aachen, Sommerfeldstr. 24, 52074 Aachen, Germany

T. Schneller (✉)
Institut für Werkstoffe der Elektrotechnik II, RWTH Aachen, 52056 Aachen, Germany
e-mail: schneller@iwe.rwth-achen.de

H. Kohlstedt · A. Petraru · R. Waser
Institut für Festkörperforschung and CNI, Forschungszentrum Jülich, 52425 Julich, Germany

J. Guo · J. Denlinger
Advanced Light Source, Lawrence Berkeley National Laboratory, Berkeley, CA 94720, USA

T. Learmonth · P.-A. Glans · K. E. Smith
Department of Physics, Boston University, Boston, MA 02215, USA

advantage of providing high flexibility with regard to stoichiometric variations including the addition of dopants [13–15].

In CSD processing a precursor solution, which contains all the metal components in form of a homogeneous solution of metallo-organic compounds, is applied onto a substrate. Followed by spin coating, evaporation, chemical reaction steps (hydrolysis, condensation), and subsequent heat treatment the initially amorphous film is transformed into a crystalline ferroelectric film. During this transformation complex rearrangement processes on atomistic and nanostructural levels take place [16]. Typically PZT films nucleate heterogeneously at the substrate/film interface [17], which leads to a columnar growth of the films and a predominant orientation of these grains either in (100) or (111) direction. The knowledge how to control this texture is of significant importance due to the anisotropic nature of the distorted PZT unit cell. It is generally agreed that highly (111) oriented PZT films on platinized silicon yield better ferroelectric properties if compared to (100) textured films [18]. Although the procedure is straightforward, the thermodynamic and chemical background is by far not well understood and often improvements are still obtained by trial and error. Especially the mechanisms of nucleation and the transformation from the amorphous film into a crystalline ferroelectric film are still a matter of debate. Among the different proposed models for the microscopic texture selection in PZT films the most prominent approach describes the (111) texture selection on platinized silicon wafers briefly as follows: (111)-oriented PZT nucleates via a transient intermetallic phase (Pt_3Pb [19], $Pt_{5-7}Pb$ [20], or $Pt_{3-4}Pb$ [21]) because of the almost identical (111) lattice parameters of the two phases PZT and Pt_xPb. It is argued that the PZT(111) texture is controlled by the formation of the intermediate Pt_xPb phase, which arises due to the reducing conditions near the interface caused by the burnout of the surrounding organic material. Recently further evidence for this model has been found by a systematic study of the influence of the precursor chemistry on the orientation and hence the electrical properties of the crystallized films [22]. The use of e.g. lead (II) propionate instead of the standard lead (II) acetate lead to PZT films with preferred (100) orientation, although the same experimental conditions have been used. It was concluded that the corresponding precursor solution has a different microscopic decomposition behavior leading to a higher oxygen partial pressure nearby the Pt/PZT interface, which in turn hinders the formation of the intermediate Pt_xPb phase. By changing from an oxidizing to a reducing atmosphere during the pyrolysis step by employing 3% forming gas, the (111) orientation of the films could be obtained again. Based on this model well oriented sub-100 nm thick PZT films with excellent electrical properties have been prepared [23, 24]. Even though these recent works give clear evidence for the intermetallic phase model, there are still unsolved questions such as how the molecular structure of the metallo organic complexes in the as-deposited film affect the microscopic reduction mechanism of lead +II to metallic lead forming the Pt_xPb phase [22]. Also the further evolution of the PZT nuclei starting from this Pt_xPb phase is unknown. Additional unsolved questions are related to the correlation of the essential ferroelectric properties (i) maximum polarization, (ii) shape of the polarization versus field hysteresis loops, and (iii) failure mechanisms (fatigue, imprint and retention) with the growth procedure during CSD processing.

A further increase of the reliability and the decrease of the necessary processing temperatures, which are of particular importance for the integration of functional ferroelectrics into the Si-CMOS technology are superior aims [4, 25]. Thus a detailed understanding of the microscopic chemical processes on the pathway from the initial precursor solution to the crystalline film is mandatory. Herewith it might be possible to achieve low-temperature processing by keeping the device performance.

For the deeper understanding of these complex mechanisms the application of advanced spectroscopy is required. Among various spectroscopic methods such as nuclear magnetic resonance (NMR) [26], or Fourier transform infrared spectroscopy (FT-IR) [27], synchrotron based methods in form of hard X-ray absorption near edge structure (XANES) [28] and extended X-ray absorption fine structure (EXAFS) [29] are appropriate spectroscopic tools to investigate the local structural environment of metal atoms in liquids, amorphous and crystalline materials. Standard X-ray diffraction (XRD) techniques with conventional X-ray tubes and hard X-ray synchrotron radiation are typically used to determine the crystal structure and phase of crystalline ferroelectric PZT powders and thin films. Since there is no long range ordering required, XANES and EXAFS have successfully been applied for PZT precursor solutions, derived gels, and films [30–33]. For example, the local structure of the Ti and Zr atoms in PZT with different compositions near the morphotropic phase boundary (MPB) has been intensively investigated with XANES by Cao et al. [34]. Therefore by the use of hard X-ray synchrotron radiation in various forms in general well established methods are available to study long range as well as local structures of complex oxide materials, such as ferroelectrics.

On the other hand soft X-ray absorption spectroscopy (XAS) and (soft)-X-ray emission spectroscopy (XES), are considered as tools with unique possibilities to probe the local *electronic* structure of materials [35–39]. In the XAS process a core electron of an atomic species is transferred by the absorption of an incident photon with an appropriate energy E into an unoccupied state in the valence band. Thus XAS probes the unoccupied Local Density Of States (LDOS) at the atomic site by taking dipole selection rules

into account. Hence only transitions to site- and symmetry-selected states with $\Delta l = +/-1$ are allowed. Accordingly, XAS results in the measurement of the partial LDOS.

Typically the XAS signal is detected in two ways, first via the total fluorescence yield (TFY) mode and second by detecting the photocurrent of the sample, known as the total electron yield (TEY) mode. Whereas the TFY monitors bulk properties due to the large photon attenuation length (100–200 nm), the short mean free path of photoelectrons (<4 nm) stemming from the sample surface, makes the TEY a surface sensitive technique [37, 40]. Interestingly, often both the TEY and TFY are monitored simultaneously. TFY is a photon-in and photon-out technique and sample charging is not a problem and makes the TFY an appropriate tool to investigate insulators as well as metals and semiconductors. In case of non-perfect insulators which allow small current flow in the range of nano Ampére, the TEY method can also be used without charging problems. In this case a sufficient grounding of a part of the sample is a necessity.

A related type of spectroscopy, called resonant inelastic X-ray scattering (RIXS), attracted considerable interest with the advent of tunable high-brilliance synchrotron light (incoming Photon flux approx. 10^{12}/s) and extremely sensitive photon detectors [35–42]. Due to these recent innovations RIXS is enabled with reasonable short integration times because RIXS is a second order process yielding extremely small signal amplitudes [41]. RIXS provides essential information about strongly correlated electron systems present in e.g. transition metal compounds and allows for studying the interplay between the local and itinerant character of 3*d* electrons. Important information about multiplet coupling, interatomic hybridization as well as electron correlation can be obtained [43, 44].

The present work concentrates on the study of the amorphous to crystalline phase transition of CSD derived $Pb(Zr_{0.3}Ti_{0.7})O_3$ (PZT) films on platinized silicon wafers by XAS, XES, RIXS, and conventional XRD, which is supplemented by scanning electron microscopy (SEM) and ferroelectric hysteresis measurements. By using soft X-ray spectroscopy additional and complementary information are expected with respect to hard X-ray XANES and EXAFS. Based on these results an improved qualitative model for the nucleation and crystallization process of CSD derived PZT thin films is developed.

2 Experimental

2.1 Synthesis of the PZT precursor solution

All manipulations have been performed under dry argon using standard Schlenk techniques. All solvents were dried with sodium, subsequently distilled, and stored under nitrogen prior to use. The 1 mol/L concentrated stock solution was prepared from dry lead (II) acetate, zirconium tetra *n*-propoxide and titanium tetra *iso*-propoxide by refluxing in *n*-propanol, distillation, stabilization with 2,4-pentanedione and redilution in n-butanol similar to the standard procedure in Ref. [22]. 15% Pb excess were added to compensate for lead loss during the thermal treatment. Details on the precursor solution synthesis and characteristics can be found elsewhere [45]. Just prior deposition this stock solution was diluted to a concentration of 0.33 mol/L and filtered through a 0.2 μm PTFE syringe filter to form the final coating solution.

2.2 Substrate preparation

A standard platinized substrate (aix*ACCT* laboratories) was prepared by using RF sputter deposition (Von Ardenne CS 500 ES) of a 10 nm Ti adhesion layer, which expands to 15 nm TiO_2 upon subsequent oxidation, followed by sputtering of a highly (111) oriented 100 nm thick Pt layer onto thermally oxidized (100) Si wafers. This stack was preannealed in a rapid thermal annealing (RTA) unit (AST SHS 100 MA) at 700 °C just before the deposition processes to get optimal interface conditions.

2.3 Thin film preparation

The films in this work were deposited in a class 1,000 clean room on a B.L.E Delta 20 photoresist spin-coater after purging with dry nitrogen starting with 500 rpm/5 s followed by 3,000 rpm/30 s. Directly after the spin-on process the 1×1 inch^2 sample was pyrolyzed at 350 °C on a hot plate (Thermolyne). This coating/pyrolysis procedure was repeated twice. After the third pyrolysis step the homogeneously coated part of the film was diced (disco DAD 320 automatic dicing saw) into four pieces of 1×1 cm^2 size each. For the synchrotron experiments one of these 1×1 cm^2 was further diced into 5 bars of 10 mm × 2 mm. To investigate the amorphous to crystalline phase transition, four samples were annealed up to different temperatures (400, 450, 500, and 700 °C). Samples crystallized at 700 °C had a PZT film thickness of around 140 nm PZT. In order to electrically characterize the PZT thin films the residual three 1×1 cm^2 sample have been annealed together with the corresponding small bars at 450, 500, and 700 °C. Platinum top electrodes were deposited onto the latter three samples by sputtering and lift-off patterning. After the lift-off process the samples have been subjected to a post anneal at 450, 500, and 700 °C, respectively. Finally a corner of each 1×1 cm^2 film is wet chemically removed to get access to the bottom electrode for electrical characterization.

2.4 Standard characterization

The film morphology was investigated by scanning electron microscopy (SEM) using a Zeiss DSM 982 Gemini instrument. X-ray diffraction (XRD) pattern were recorded with a Philips X-Pert system with Cu Kα radiation, $\lambda = 1.5405$ Å, to detect the crystal structure and texture of the films. To roughly evaluate the degree of orientation the relative peak intensity $I_{rel}(111)$ of the (111) reflection, which was calculated according to the equation $I_{rel}(111) = I(111)/\{I(001) + I(100) + I(101) + I(110) + I(111)\}$, was determined. Since in the XRD's of most of the samples negligible intensities for the (101) and the (110)-planes occur, these lattice planes were typically not considered for the calculations.

An aixACCT TF-Analyzer (aixACCT Systems GmbH) was used to measure the hysteresis loops of the prepared films at a frequency of 100 Hz.

2.5 Soft X-ray measurements

The XAS and XES experiments were performed at the high-resolution undulator beam-line 8.0 at the Advanced Light Source (ALS), Lawrence Berkeley National Laboratory [46]. The beam-line was equipped with a spherical grating monochromator (SX-700). The spot size of the synchrotron beam was approximately 0.2×2 mm^2 at the sample side. The samples were mounted in a way that the longer side of the beam spot (2 mm) was parallel to the longer side of the each sample (10 mm). The sample surface normal was at an angle of 40° relative to the incident X-ray beam axis. The total electron yield (TEY) was monitored by the photocurrent of the sample in dependency of the incoming photon energy. Each sample was grounded at the edges with conductive silver paste. The TFY signal was collected by negatively biased channeltron. The RIXS emission signal was recorded via a high-resolution Rowland circle type grating spectrometer with an energy resolution of about 0.3 eV. The Ti $L_{2,3}$-, the O *K*- and C *K*-edge absorption spectra were investigated near the 457, 530, and 283 eV threshold energies, respectively.

3 Results and discussion

In the following paragraph the results of the standard characterization for the morphological and electrical properties of the samples are presented.

3.1 Standard characterization

3.1.1 XRD

To check the phase and orientation at first all samples were subjected to X-ray diffraction in the theta-2-theta modus. Figure 1 shows the diffractograms of the five films. In all samples a very strong reflection at 39.9° corresponding to the (111) texture of the Pt bottom electrode is observed. The sample pyrolyzed at 350 °C without further thermal treatment is X-ray amorphous as expected. Already the 400 °C annealed sample exhibits a very small feature at 22° corresponding to the (100) orientation of PZT which becomes significant for the diffraction pattern of the 450 °C annealed sample ($I_{rel}(111) = 0.27$). Such samples develop a predominant (100) orientation (XRD pattern not shown here) by further annealing at 700 °C. In contrast to the sample annealed at 450 °C the sample which was annealed at 500 °C on a hot plate features a strong (111) orientation ($I_{rel}(111) = 0.70$). The same situation is found for the sample crystallized at 700 °C ($I_{rel}(111) = 0.65$). These interesting findings are basically in agreement with earlier studies which conclude that the pyrolysis conditions of the as-deposited films have a strong impact on the texture selection of PZT thin films [47–49]. Hence temperatures around 450 °C promote the (100) oriented growth while films pyrolyzed at around 350 °C promote the (111) oriented growth. Interestingly, this behavior was also found in the literature in the case of a similar precursor chemistry [47, 49].

An important difference to these earlier investigations however is that the onset of the crystallization process is at somehow lower temperature in the present case as can be seen in Fig. 1. The film annealed at 450 °C showed already a well defined perovskite phase in the XRD while the PZT film at the morphotropic phase boundary investigated in Ref. [49] was still amorphous at this temperature. The reason might be that the higher content of the refractory material zirconia in the latter case delays the crystallization process to higher temperatures.

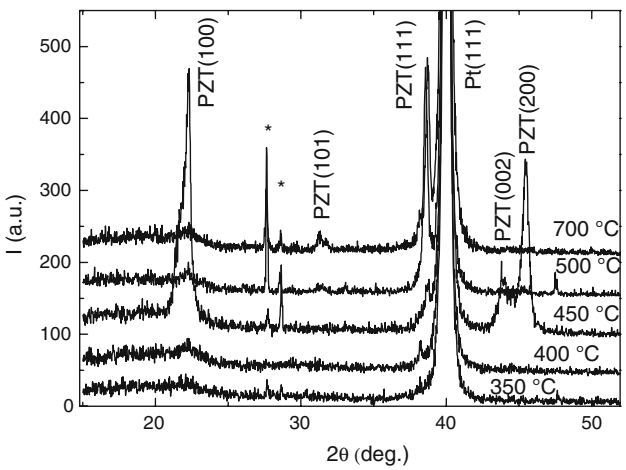

Fig. 1 X-ray diffraction pattern (theta-2-theta mode) for the 5 samples heat treated at different temperatures as indicated. The asterisks denote reflections of the substrate

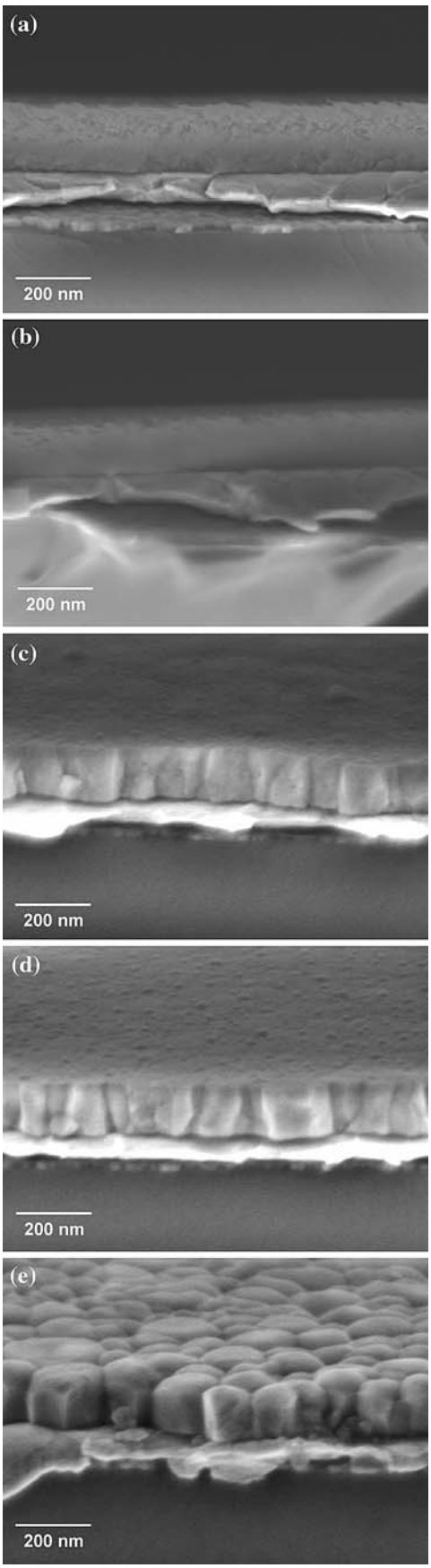

Fig. 2 Cross section scanning electron micrographs of the differently heat treated samples ordered by increasing temperature, namely (**a**) 350 °C, (**b**) 400 °C, (**c**) 450 °C, (**d**) 500 °C, and (**e**) 700 °C. The amorphous samples (**a**) and (**b**) have a featureless microstructure. The columnar microstructure takes more and more shape upon increasing annealing temperatures (samples (**c**–**e**))

This means that in the temperature range between 350 and 450 °C of the present study significant microscopic changes nearby the Pt/PZT-interface in the initially X-ray amorphous film must occur leading to nucleation seeds which are either (100) oriented or (111) oriented. By applying a steep heating ramp (hot plate or RTA) to higher temperatures the once formed nuclei grow according to this predefined orientation on the cost of the X-ray amorphous environment.

3.1.2 SEM

From the samples heat treated at different temperatures cross-section SEM images were taken (Fig. 2). Increasing temperatures led to a decrease of the film thickness from the as-pyrolyzed film (approx. 210 nm) to the fully crystallized film (approx. 140 nm) due to the increasing densification of the films. The 350 and 400 °C heat treated samples had a featureless microstructure corresponding to the X-ray amorphous nature of these films. By increasing the annealing temperature the films took more and more form. Already the 450 °C showed a columnar microstructure (Fig. 2c) which ends up in well defined grains of ∼70-170 nm lateral size in the film crystallized at 700 °C (Fig. 2e).

3.1.3 Electrical characterization

In order to evaluate the films with regard to their basic ferroelectric properties remanent polarization (P_r) and coercive voltage (V_c) 1 × 1 cm^2 samples were prepared at those temperatures were crystallinity can be expected from the XRD data. Hence samples at 450, 500 and 700 °C were prepared in parallel to the bars for the synchrotron experiments. In addition, two 1 × 1 $inch^2$ sample heat treated at 350 and 400 °C have been prepared according to the same process than the corresponding bar samples. Figure 3 shows the results of the hysteresis measurements.

Both X-ray amorphous samples (350 and 400 °C) show no polarization. In agreement with the crystalline nature of the samples annealed at higher temperatures, typical hysteresis curves are measured (Fig. 3). However they differ significantly in the value of the remanent polarization and the shape of the loop. While the fully crystalline and highly (111) oriented film (700 °C) shows a square hysteresis loop with high remanent polarization (Pr ∼ 34 μC/cm^2), the loop of the also (111) oriented film annealed at 500 °C

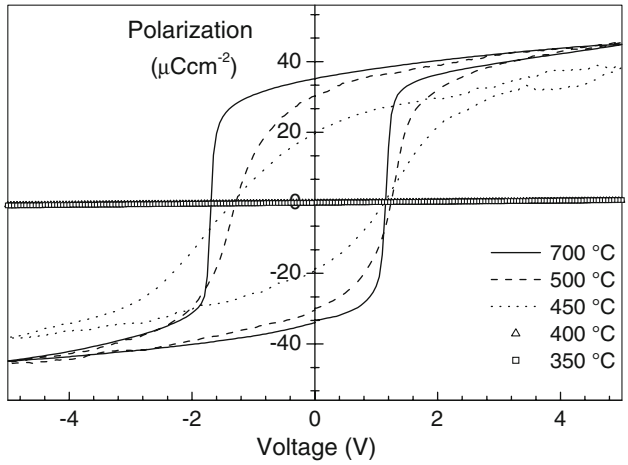

Fig. 3 Hysteresis loops of the samples heat treated at 450, 500, and 700 °C as indicated in the graph. All three samples show a well saturated hysteresis loop. The lowest remanent polarization is observed for the predominantly (100) oriented film in accordance with the literature [18, 22]. The two X-ray amorphous samples (350 and 400 °C) have been prepared extra for comparison. As expected they show no polarization corresponding to the non-crystalline character

shows a slightly lower Pr of $\sim$30 μC/cm^2 but a bit more slanted shape. This can be explained in terms of a not fully crystalline film where amorphous areas surround the crystalline PZT grains which lead to a lower volume fraction of switchable ferroelectric material and interface dead layer [2]. The decrease of remanent polarization (Pr $\sim$ 19 μC/cm^2) and the inclination of the hysteresis loop is even more pronounced in case of the 450 °C annealed film. A further reduced number of switchable PZT grains due to the predominantly in-plane orientation of the PZT grains and residual amorphous areas as well as residual carbon (see Sect. 3.3) are the reason for this behavior.

In order to get further insight into the microscopic chemical changes, soft X-ray spectroscopy has been applied and the results are discussed in the following paragraphs. Interestingly it has been noticed that the as-pyrolyzed sample (350 °C) degraded under synchrotron radiation after 20 min. Nevertheless, the short measurement intervals of 5 min. and less, as in case of XAS, enabled reasonable non-destructive experiments. However for RIXS typical acquisition times are in the order of 1–2 h. After 30 min radiation on the 350 °C sample, black traces at the beam spot on the sample have been observed. Simultaneously a tremendous distortion of the Ti of the XAS and RIXS spectra were observed. Samples annealed at temperatures of 400 °C and higher never featured this behavior. It is suggested that the amorphous state in addition with the relatively large carbon content are the reasons for the radiation instability of the 350 °C sample. Therefore in the following the efforts are concentrated on the 400 and 700 °C samples.

3.2 Titanium Ti $L_{2,3}$ absorption and emission spectra

In Fig. 4 the X-ray absorption spectra simultaneously detected by the total electron yield (Fig. 4a) and the total fluorescence yield (Fig. 4b) are shown. For the 700 °C samples, we observed four (see labels in Fig. 4a Ti upper spectrum, 700 °C) prominent peaks which are related to the

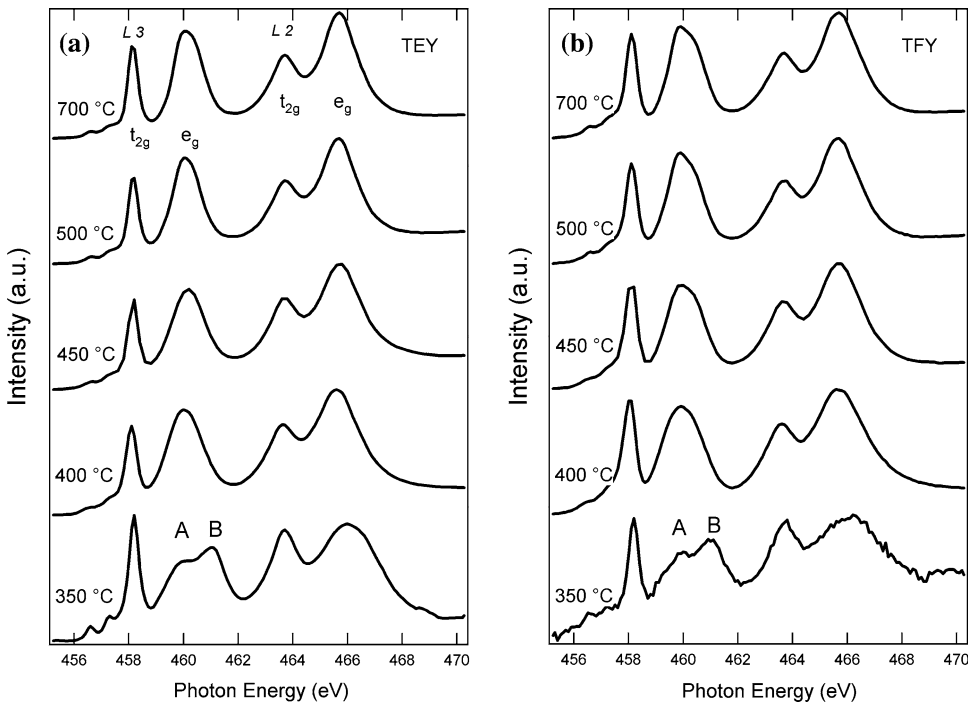

Fig. 4 Ti 2p XAS spectra of PZT for different maximal annealing temperatures. The crystal field splitting t_{2g} to e_g (10 Dq) is marked for the $2p_{3/2}$ ($L3$) and 2 $p_{1/2}$ (L_2) core levels; TEY (**a**), TFY (**b**)

crystal field splitting of Ti^{4+} in an octahedral symmetry. The first two peaks (at 458 and 460 eV) belong to the $2p_{3/2}$ (t_{2g} and e_g) and the third and fourth peak (464.35 and 466.7 eV) belong to the $2p_{1/2}$ (t_{2g} and e_g) transitions [50–54]. Since the splitting between t_{2g} and e_g is related to the crystal structure, it may basically further change upon the change of the lattice constant. Existing studies show that the shape of e_g is sensitive to the crystal structure of TiO_2 (Anatase [55] and Rutile [56]). A further splitting of e_g at the L_3-edge is due to the different Ti–O bonding length, and the intensity ratio between these two e_g-related peaks varies correspondingly to the anatase and rutile phase as will be also described below.

In addition, the TEY's and TFY's are rather similar for all annealing temperatures which indicates equivalent bulk and surface properties.

It is interesting to note, that even in a low temperature grown PZT film (400 °C) the Ti ion crystal field environment was *not* considerably different to that of the samples grown at higher temperature (700 °C), whereas the 350 °C sample (see Fig. 4 lower spectra) showed a splitting of the $2p_{3/2}$ e_g peak with 2 peaks, one at 460 eV (A) and the second one at 461 eV (B). Peak A is roughly 10% lower in intensity than peak B.

This particular feature corresponds to a Ti^{4+} ion in the rutile type structure (D_{2h}) with a slight distortion from the O_h symmetry. In the anatase phase, Ti shows an opposite intensity distribution (peak A larger than peak B) [53, 54, 57]. Because anatase is typically the low temperature phase one would first expect an anatase structure for the 350 °C sample. Indeed the enthalpies for bulk titanium dioxides ΔH_f follow the trend: ΔH_f rutile $>$ ΔH_f brookite $>$ ΔH_f anatase, whereas for the surface energy shows the opposite relation [58]. Therefore, depending on the particular growth conditions for thin films, all titanium dioxide modifications can be expected. Ti in a rutile and anatase environment has been also observed in $CoTi_{1-x}O_{2-\delta}$ films grown by pulsed laser deposition in dependency on the growth conditions [53, 59]. Roughly speaking, they observed at elevated temperatures (700 °C) and elevated oxygen partial pressure (10^{-3} Torr or more) a stabilization of the Ti in the anatase structure. While at low deposition temperatures of about 550 °C or low partial oxygen pressure ($<10^{-5}$ Torr) the rutile type double peak (peak B higher then peak A) was observed. This fact was also observed in case of other thin film Ti-oxide compounds grown by pulsed Laser deposition (PLD) [60]. The rutile phase was also found by Muralt et al. for sputtered PZT films [61].

Now we turn to the resonant Ti $L_{2,3}$ fluorescence spectra recorded at the Ti 2p threshold [55, 62]. Here the photon excitation energy is tuned to particular energies at the Ti $L_{2,3}$ edge. The individual excitation energies are labelled

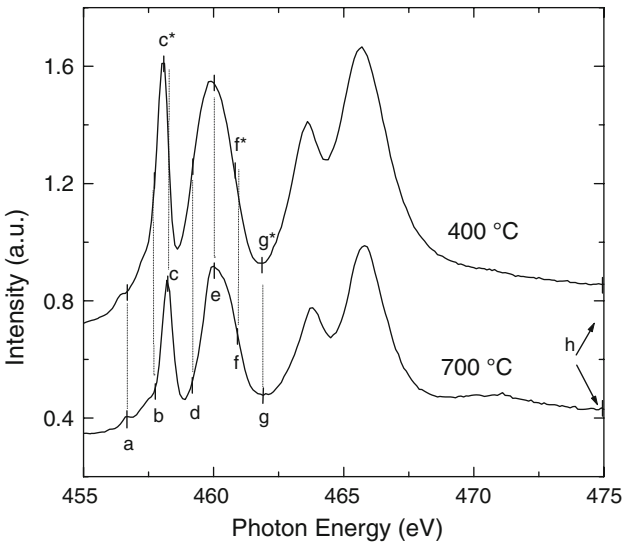

Fig. 5 Ti 2p XAS spectra (TFY) of two PZT thin film samples annealed at 400 °C (top spectrum) and 700 °C (bottom spectrum). TFY was measured in order to label the excitation energies by a-h for the RIXS measurements (see Fig. 6)

(by letters a–h) and are shown in Fig. 5 for the 400 °C (top curve) and 700 °C (bottom curve) sample.

Small energy deviation between the excitation energies of the 400 and 700 °C samples are named by c*, f* and g*. In Fig. 6 the RIXS data are displayed for various resonantly excited states for the 400 and 700 °C samples, respectively. In the low and high temperature samples, RIXS features were observed at 3 eV below the excitation energy. While *dd*-excitation is basically an on-site electronic excitation localized at the Ti atom (ion), charge transfer (CT) excitation would be an electronic excitation from Ti 3d to O 2p or vice versa. Typically, CT-excitation appears at a higher energy loss than *dd*-excitation. In Ti compounds, RIXS spectra would reveal *dd*-excitations at around 1–3 eV when Ti is in the 3+ oxidation state (with $3d^1$), while Ti^{4+} typically gives no *dd*-excitation features. The CT-excitation would be typically at 3 eV and above. Hence the inelastic contributions were assigned as CT-excitations from occupied O 2p states to unoccupied Ti 3d states. It is known that the $3d^0$ configurations are considerable mixed with the CT-configurations by strong Ti 3d–O 2p hybridization. There are radiative transitions to different final states. Earlier X-ray emission studies identified features 4 eV below the elastic peak as CT-excitations. It has been shown that the RIXS structures of 3d transition metal (M) $L_{2,3}$ spectra reflect *dd* transitions and O *2p*–M *3d* CT-excitations [63, 64]. Similar RIXS origin is expected for $PbZr_{1-x}Ti_xO_3$ due to the significant degree of localization of Ti *3d* states. The relative intensity of the recombination peak (*E*) decreased with increasing excitation energy. More interesting is the strong dependence of the RIXS spectra on the

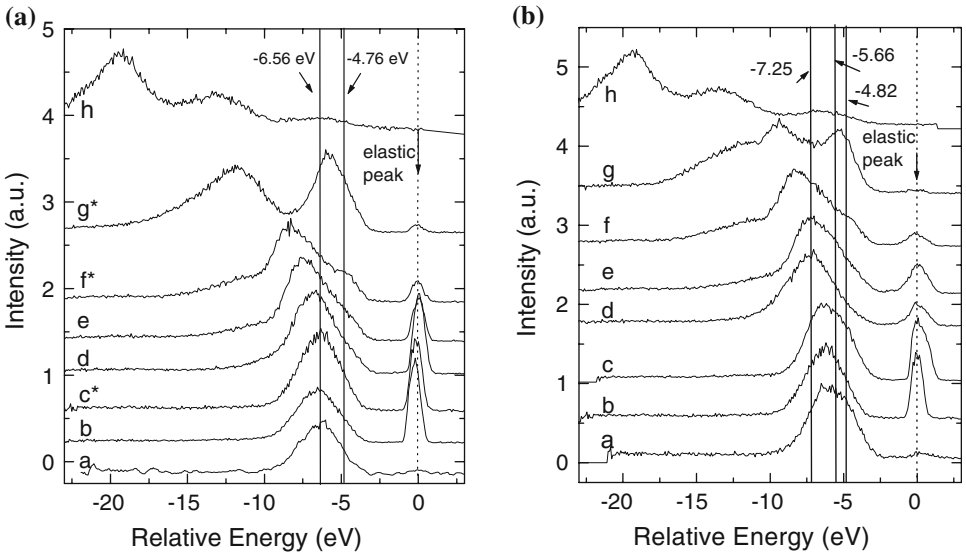

Fig. 6 (**a**) Experimental Ti $L_{2,3}$ RIXS data on the PZT 400 °C sample excited at the incident-photon energies a–h which are indicated in the Ti absorption spectrum in Fig. 5 (top spectrum), (**b**) Experimental Ti $L_{2,3}$ RIXS data on the PZT 700 °C sample excited at the incident-photon energies a–h, which are indicated in the Ti absorption spectrum Fig. 5 in the (lower spectrum)

excitation energy. The RIXS spectra consist of resonant and non-resonant parts that can be easily identified. The non-resonant features appear at the constant energies with an enhanced intensity upon the excitation energies. The resonant part follows the excitation energy due to energy conservation since the emitted photon energy must increase with increasing incident photon energy. This gives rise to loss features with a constant difference in energy below the recombination. 400 °C shows CT-excitations at 4.76 and 6.56 eV (Fig. 6a), while 700 °C shows CT-excitations at 4.82, 5.66, and 7.25 eV (Fig. 6b).

3.3 Oxygen K absorption and O K emission spectra

In Fig. 7 the O 1s XAS for the five samples are shown. The TEY (Fig. 7a) and TFY (Fig. 7b) were simultaneously acquired between 524 and 565 eV. The O 1s spectra are related to unoccupied O p-states mixed in the conduction band [38]. Consequently, these spectra represent, due to the metal-oxygen hybridization, the unoccupied bands of Ti and Zr in the oxide and are different to the Ti 2p absorption spectra which reflect the $2p^6 3d^n \rightarrow 2p^5 3^{n+1}$ transitions [50]. Above the O *K*-edge it is convenient to divide the spectra into two energy regions. The first one from 532 eV $< E_{photon} =$ 537 eV the second from 537 eV $< E_{photon} >$ 560 eV. To get some inside about the local electronic structure in the present samples, at first the results with TiO_2 as a reference are compared for the TEY measurement (Fig. 7a).

The interval from the threshold up to approximately 537 eV is related to O 2p states which are hybridized with the Ti 3d states in the conduction band (CB) and are split into the well known t_{2g} and e_g sub-bands in case of polymorph TiO_2. The ligand field splitting for the as-pyrolyzed sample (350 °C, Fig. 7a) of 3.0 eV corresponds well to the rutile phase, which is in agreement with the findings for the Ti XAS in Sect. 3.2. The higher energy range from 537 eV up to 560 eV is attributed to the O 2p states hybridized with the Ti 4 sp or other counter-ion bands. It is known that these peaks are more sensitive to long-range order [50]. In the following the present O 1s spectra are compared with results from the literature.

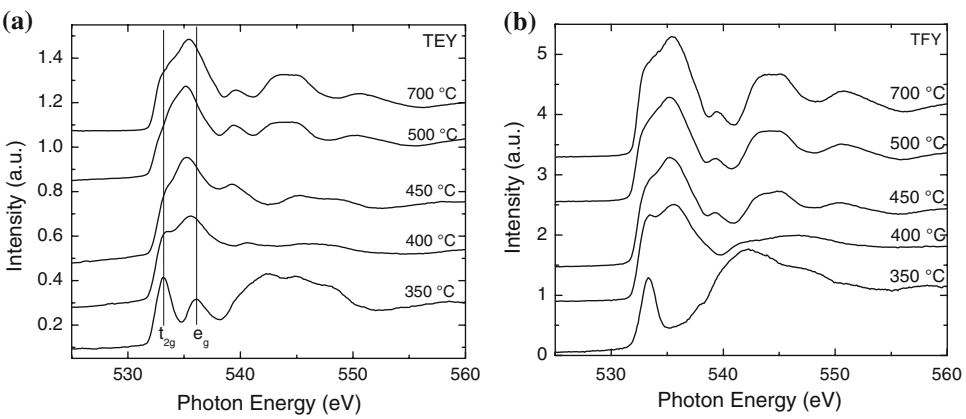

Fig. 7 O 1s XAS spectra of PZT of all samples; TEY (**a**), TFY (**b**). Please note that these spectra were not calibrated and have in principle to be shifted by −2 eV. However the absolute value has no influence on the interpretation in context to the present paper

The TEY in Fig. 7a of the low temperature sample (350 °C, lower spectrum) is the only one which shows similarities to rutile polymorph TiO_2 [54]. The bulk sensitive TFY exhibited considerable deviations. First, the second peak at about 536.1 eV (as easily seen in Fig. 7b) is disappeared. Moreover, also in the higher energy region, there are clear differences between the TEY and TFY spectra. For higher annealing temperatures both, the TEY and TFY spectra emerge more and more. For the sample annealed up to 700 °C, both spectra are equivalent, indicating the tendency that the bulk and surface properties became similar in the crystalline sample. These differences might be explained by different amounts of carbon–oxygen species present in the surface and volume of the as-pyrolyzed film. The carbon in the as-pyrolyzed film reacts at first in the surface near region with the oxygen from the air environment. Since the pyrolysis is stopped after 2 min, the film is in a quenched state with a carbon rich bulk region and a more oxidized surface region. Hence the surface sensitive TEY spectrum corresponds to a rutile phase environment. Due to the carbon rich bulk phase of the film it is likely that the oxygen TFY spectrum has strong contributions of carbon–oxygen species which leads to a significantly different TEY and TFY spectrum. This difference was not found for the titanium TEY and TFY spectra (see Sect. 3.2, Fig. 4) because the local titanium environment is dominated by the oxygen octahedra rather than by the carbon.

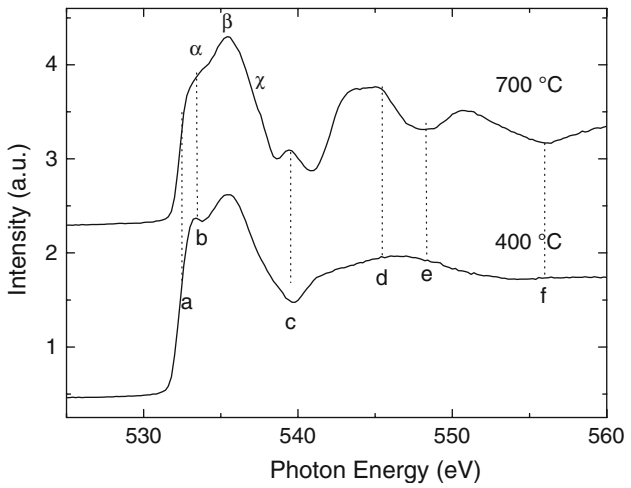

Fig. 8 O 1s XAS spectra of two PZT thin film samples annealed at 700 °C (top spectrum) and 400 °C (bottom spectrum). The excitation energies are labelled by a–f for the 400 and 700 °C samples and significant features are labelled by α, β, and χ for the 700 °C sample

The XAS of the 700 °C sample at the O 1s edge exhibit in the energy range between 530 and approx. 544 eV a spectrum which shows the same features as those presented by Higuchi et al. [65]. They deposited $Pb(Zr_{0.65}Ti_{0.35})O_3$ by MOCVD on (100) MgO substrates. By following the theoretical work of Cohen and Krakauer [66] based on the all-electron, full-potential, linearized augmented plane wave method (in the local density approximation (LDA)) as well as the experimental work from Higuchi et al. [65], the peaks labelled by α (531 eV), β (532 eV) (see Fig. 8 upper curve (O 1s XAS, 700 °C)) consist of the Ti 3d state hybridized with the Pb 6p state. Higuchi observed at 2.5 eV above the threshold a clear shoulder (marked by χ) and interpreted this feature by the Zr 4d state hybridized with the Pb 6p state. There is no pronounced peak at the χ position visible in Fig. 8.

The excitation energies are labeled by a–f in Fig. 8. The corresponding RIXS are shown in Fig. 9a, b for the 400 and 700 °C sample, respectively. Two significant features are marked by A and B in Fig. 9b. These two peaks are related to the Ti 3d state hybridized with the O 2p state. The peak A corresponds to the nonbonding state and peak B corresponds to the bonding state, which is mixed with the Ti 3d state [65]. The Ti–O hybridization effect has been found as well in $BaTiO_3$ and $SrTiO_3$ compounds [65–69]. In case of the 400 °C sample (Fig. 9a), the RIXS shows also a strong peak A, whereas the feature B is not visible for the excitation energy a (532.5 eV). At higher excitation energies (b–f) feature B could be identified by a shoulder.

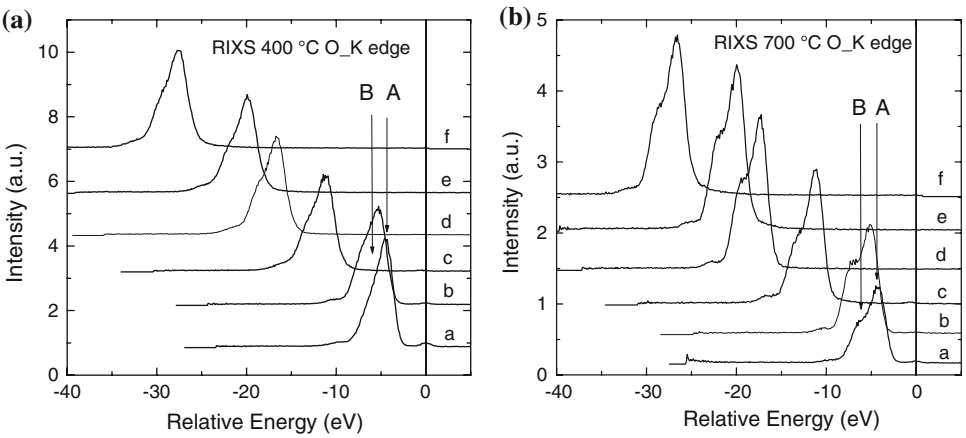

Fig. 9 Measured O *K* RIXS data for the PZT 400 °C (**a**) and 700 °C (**b**) samples. The labels correspond to the excitation energies marked by a–f in Fig. 8 with $a = 532.5$, $b = 533.45$, $c = 539.5$, $d = 545$, $e = 548.3$, and $f = 556$ (all in eV)

3.4 Carbon K edge absorption

With respect to the above presented Ti and O XAS and XES investigations, carbon might behave rather different in the PZT films. Carbon in chemical deposition methods (such as MOCVD or CSD) is a mandatory ingredient for the metal(lo) organic (liquid) precursor solution. However although carbon is essential for the deposition process it should be completely removed by formation and evaporation of CO_2 and H_2O during the annealing procedure to achieve finally an ideal Perovskite structure (ABO_3). In contrast to the elements Ti, Pb and O a drastic decrease of the carbon content during annealing is expected. The carbon chemistry in CSD derived PZT thin films during the nucleation and the amorphous to crystalline phase transition is almost unknown. On the other hand it was figured out by many researchers [19–24] that a certain amount of carbon during pyrolysis is important to generate reducing conditions nearby the platinum/PZT interface which leads to the reduction of Pb^{2+} to Pb^0. The latter forms the (111) textured growth promoting Pt_xPb intermetallic phase. XAS and RIXS might offer an opportunity to shed more light on the role of carbon in wet chemically deposited PZT thin films. Although the carbon 1s edge has been extensively studied by XAS and RIXS in its various configurations (e.g. diamond, graphite, fullerene, amorphous, or HOPG (Highly Oriented Pyrolytic Graphite)) this is not a simple task. In the present work, carbon is solved in the PZT films in an unknown way, and in addition, in various concentrations in dependency of the annealing temperature which hinders a straightforward interpretation of the spectra. More about the chemistry in carbon and its various modifications can be found for example in Ref. [41, 70, 71].

In Fig. 10a, b the series of TEY and TFY spectra of the five samples (350–700 °C) are shown at the C 1s edge, respectively. As expected, the amount of C in the film decreases drastically reduced from the sample 350 °C to that of 700 °C. At 450 °C already most of the initial carbon from the precursor solution is vaporized. For the spectra at 350 and 400 °C the TEY and TFY are considerably different. This reflects the fact that carbon is inhomogeneously distributed. For films annealed to 450 °C and higher there is clear tendency that the TEY and TFY signals emerge (together with the reduction in signal intensity).

In case of the 350 °C sample at 282 and 283 eV in the TEY and TFY strong signals were observed. For higher excitation energies two further peaks (between 284.5 and 287 eV) are visible followed by a long, featureless tail up to 300 eV. The 282 and 283 eV peaks might correspond to the π^* orbital level. The 400 °C sample showed a significant peak in the TFY at 288 eV which is may be related to the σ^* orbital energy. For the following samples annealed above 400 °C the carbon signal is considerable suppressed and indicates the strong carbon loss with increasing annealing temperature. This spectrum is very similar to those of amorphous carbon. Interestingly, the TEY from the 400 °C sample up to 700 °C sample exhibited this features and means that the upper most carbon layer during the vaporisation is amorphous. More investigations are necessary to clarify the complex carbon chemistry during the amorphous to crystalline phase transition PZT films. However the observed relatively high amount of carbon in the as-pyrolyzed sample is a clear qualitative hint to reducing conditions in the interface region which is one precondition for the model proposed in the next section.

3.5 Proposed model for texture formation

In this section a possible explanation will be given how the findings of this study could be matched with current models for the texture selection of CSD derived PZT thin

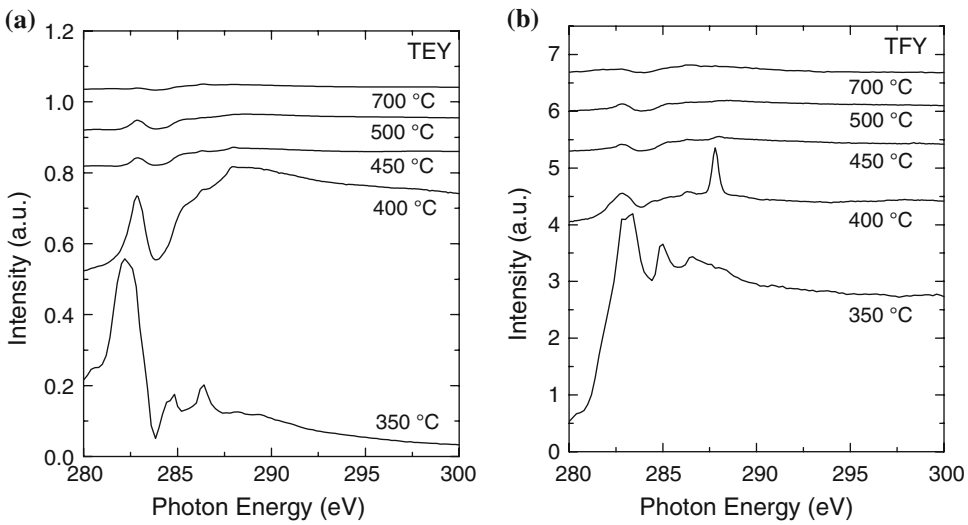

Fig. 10 Series of TEY (**a**) and TFY (**b**) spectra at the C 1s edge of all five samples (350–700 °C)

films. Since amorphous PZT films in principle transform by a nucleation-controlled mechanism [17] into a columnar grown perovskite phase one has basically to consider the conditions at the interface. As already briefly described in the introduction, the most prominent model for the (111) texture selection in CSD derived PZT thin films on bare platinized silicon wafers is based on the formation of a transient intermetallic Pt_xPb ($x = 3$ [19], 5–7 [20], or 3–4 [21]) alloy, whereby the exact composition is not clear and quite difficult to obtain. It has also been reported that a Pt_3Ti alloy, which is formed on $Pt/Ti/SiO_2/Si$ substrates by Ti outward diffusion and reaction with Pt, decreases the interfacial energy between Pt electrode and PZT(111) planes, due to the close lattice matching similar to the intermediate Pt_xPb phase [72, 73]. The formation mechanism of a Pt_3Ti alloy can be ruled out in the present study because of the use of a TiO_2 adhesion layer for the platinized silicon substrate. Titanium dioxide does not diffuse along the platinum grain boundaries as it was shown in the literature [74]. This is also supported by recent results where the use of Al_2O_3 and ZrO_2 adhesion layers did not inhibit the (111) nucleation of PZT [22].

Beside the intermetallic seeding models some researchers state that a direct nucleation of PZT due to the lattice matching between PZT(111) and Pt(111) at the film/Pt interface [75–77] takes place. Certainly this is an obvious approach but it cannot explain the matter of fact that there is a difficulty to maintain the (111) orientation, if the film thickness gradually decreases below 100 nm although the same precursor solution and process are used [23, 24]. However the Pt_xPb model gives a reasonable explanation for this result and also the hint to solve this problem. If one takes into account that reducing conditions, caused by the burnout of the organic material, nearby the Pt/PZT interphase, can only be maintained if the diffusion of oxygen is sufficiently slow, then it becomes clear that the thickness of the amorphous film must be above a certain threshold. If the film is too thin which means some 10s of nm below 100 nm, at the interface oxidizing conditions are present and the reduction of Pb^{2+} to Pb^0 cannot take place. Thus the Pt_xPb alloy cannot form and a predominant (100) orientation is obtained.

By using a reducing atmosphere the intermetallic phase can form again and the (111) orientation of films down to 30 nm was obtained again [24]. Consequently excellent square hysteresis loops with $P_r > 30\ \mu C/cm^2$ could be recovered. Said intermetallic phases can be also obtained in case of MOCVD processes [78]. In the latter case these phases often become very dominant which can be explained by the even stronger reducing conditions in the MOCVD process compared to the CSD process which may lead to the situation that the amount of the formed Pt_xPb-phase is to high and cannot be easily reoxidized.

From all these considerations it is concluded that the formation of the transient intermetallic Pt_xPb alloy, as one of the first steps of the nucleation in CSD derived PZT (111), is most likely. An optimized CSD process seems to be a tradeoff between a sufficient amount of transient intermetallic phase to promote the (111) nucleation and not too high amount to be completely reoxidized during crystallization. The next steps in the nucleation mechanism were not clear so far.

On the other hand it is known that sputtered thin i.e. $\sim$2 nm TiO_2 films act as seed layers on bare Pt (111) [61]. They promote a (111) oriented growth of sputter deposited as well as of CSD derived PZT thin films. The working principle was explained in terms of an epitaxial relationship between strained rutile (110) and Pt (111). It was stated that the oxygen rows of the rutile surface work in favor of a PbO_3^{4-} (compare Fig. 11) coverage. Thus on top of this rutile seed layer the (111) textured perovskite nucleates epitaxially i.e. in (111) direction. Muralt et al. also pointed out that a non-oriented or amorphous TiO_2 layer fails to act as seed layer [61].

In the present study no artificial TiO_2 seed layer is used on top of the Pt. In addition we can exclude Ti diffusion from the adhesion layer towards the Pt surface as discussed above. However we found TiO_2 in the rutile phase already in the as-pyrolyzed film at 350 °C by the XAS experiments (see above). Thus the (111) PZT nucleation mechanism might be basically explained by an extension of the known intermetallic phase layer model [19–21]. If one takes into account that the lattice constant of the (111) Pt_xPb-phase is very similar to that of (111) Pt it is assumed that the detected rutile in the as-pyrolyzed film, could also grow epitaxially in (110) direction on top of this Pt_xPb-alloy (Fig. 11).

In the next step this rutile surface facilitates the epitaxial coverage with PbO_3^{4-} very similar to sputtered ultrathin TiO_2 seed layers. Upon further processing by fast heating ramps (hot plates or RTA) to temperatures of 500 °C and above, these seeds grow further in the (111) direction forming the columnar grown perovskite films. During the oxidizing annealing conditions the incipiently formed Pt_xPb alloy is reoxidized and the resulting Pb^{2+} is incorporated into the perowskite lattice after slight displacement of the oxygen and titanium ions, as schematically indicated in Fig. 11.

Until now the model only explains the (111) texture selection. In order to explain the observed temperature dependent competition between a predominant (111) texture ($T \geq 500$ °C) and the (100) orientation ($T = 450$ °C), which is in agreement with the literature [47, 49, 79], the following has to be considered. Basically the case of (100) oriented growth of PZT films is often explained by an energetically favored (100) growth plane [76, 80, 81] and

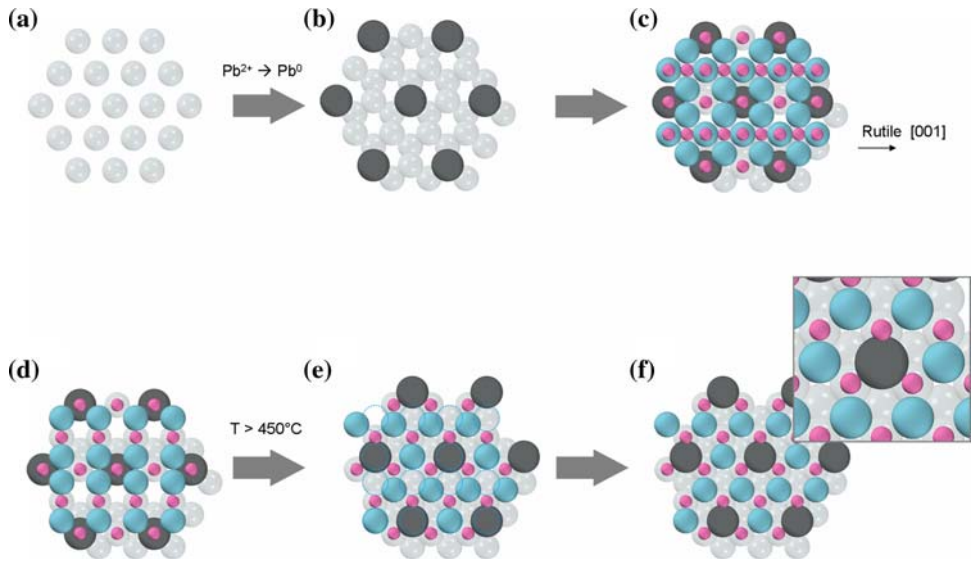

Fig. 11 Schematic representation which illustrates the first nucleation steps of $PbTiO_3$ on (111) oriented platinum. (**a**) Shows the hexagon surface of (111) plane of the bare Pt; (**b**) after reduction of Pb^{2+} to Pb^0 the intermediate (111) $PbPt_x$ alloy is formed (light grey sphere = Pt; dark grey sphere = Pb. (**c**) On top of this $PbPt_x$ layer strained rutile (blue spheres = oxygen and small magenta spheres = titanium) is stacked (the (001) direction of rutile is given by the arrow and some out off plane oxygen and titanium ions from the rutile structure are also shown). (**d**) Shows only the first layer of oxygen and titanium ions of the rutile layer in order to facilitate the next proposed step of the nucleation process. During further fast heat treatment to temperatures of above ~450 °C in oxidizing atmosphere, the Pb^0 in the $PbPt_x$ layer is oxidized to Pb^{2+} which is associated with a small outwards displacement from the plane of Pt into the 1st plane of the strained rutile layer. In the latter further relatively small displacements of O and Ti (not displayed) have to take place; (**e**) shows the situation after the reoxidation of Pb and the various displacements. The blue scattered circles indicate the original positions of the oxygen ions; (**e**) the enlarged inset shows the hexagon of the PbO_3^{4-} plane of (111) oriented lead titanate. These seeds grow further also by introduction of Zr to form finally columnar (111) oriented PZT thin films

PbO seed layers or (001) oriented PbO seed crystals which allow for a preferred (100) texture evolution of PZT due to good lattice matching [79, 82–84]. The formation of PbO seeds or seed layers within the intermediate Pt_xPb seed layer model is explained by Chen and Chen [79] by a kinetic consideration. If the as-pyrolyzed film is annealed for longer times at temperatures where the PZT formation is very slow, the initially formed Pt_xPb alloy will reoxidize to PbO giving the seed layer for (100) PZT as described above. During further heat treatment these films crystallize in (100) direction. If as-pyrolyzed films are directly annealed at higher temperatures, e.g. 500 or 700 °C, the perovskite forms rapidly on the initially formed (111) oriented nuclei (see above) and hence the (111) orientation dominates.

4 Conclusions

The transition of CSD derived tetragonal PZT thin films from the amorphous as-pyrolyzed state to the crystalline perovskite has been studied by soft-X-ray spectroscopy. Interestingly the local titanium environment of the as-pyrolyzed sample was found to be rutile type which is normally the high temperature modification of titanium dioxide. Thereby the spectra of the bulk sensitive TFY method and the surface sensitive TEY method have the same feature which shows that there is no difference between bulk and surface. The oxygen environment of the as-pyrolyzed sample however shows significant differences with regard to surface and bulk properties. While the surface sensitive TEY spectrum again shows the feature of the rutile structure the TFY spectrum representing the bulk of the film is superposed by oxygen species containing carbon, which can be explained by a quenched state with a carbon rich bulk region and a more oxidized surface region. This is also reflected in different TFY and TEY carbon K edge absorption spectra. The residual carbon in the bulk of the as-pyrolyzed samples enables a reducing environment in the Pt/PZT interface region, which in turn is a precondition for formation of an intermediate $PbPt_x$ alloy. A qualitative model based on the combination of well known models for the nucleation of (111) oriented PZT and the matter of fact that rutile has been found by XAS was discussed. Titanium dioxide in rutile form stacks at first on the $PbPt_x$-phase due to excellent lattice matching and forms by slight movement of the ions the (111) PTO nuclei which grows to (111) oriented columns of PZT upon fast heating to 500 °C or temperatures above. The predominant (100) orientation of the 450 °C annealed film

might be explained by a literature known kinetic consideration. Thus a slow perovskite formation at this temperature leeds to the generation of PbO seeds or seed layers by the oxidation of the intermediate $PbPt_x$ phase, which promote the (100) growth.

In accordance with the literature, the highly (111) textured samples show a superior ferroelectric behavior compared to the predominantly (100) oriented samples. A strong competition in texture selection was found in the temperature range from 400 to 500 °C. By application of 450 °C the films grow predominantly in (100) direction while a crystallization temperature of 500 °C and above leads to (111) textured films.

Acknowledgements We thank the Volkswagen-Stiftung (Project: "Nanosized Ferroelectric Hybrids") and the Deutsche Forschungsgemeinschaft for financial support. N.V. acknowledges funding from the ARC Discovery Project DP0666231. The authors would also like to thank R. Thelen for sample preparation, D. Erdoglija for preparation of the electrodes, G. Wasse for SEM and T. Pössinger for the graphics. One of us (H. Kohlstedt) thanks the members of the Advanced Light Source and the UC Berkeley for a very fruitful and pleasant stay in Berkeley between 2005 and 2006. The Boston University program is supported in part by the DOE under DE-FG02-9845680.

References

1. Scott JF, Araujo CAPd (1989) Science 246:1400
2. Scott JF (2000) Ferroelectric memories. Springer Verlag, Berlin
3. Ahn CH, Rabe KM, Triscone J-M (2004) Science 303:488
4. Setter N, Damjanovic D, Eng L, Fox G, Gevorgian S, Hong S, Kingon A, Kohlstedt H, Park NY, Stephenson GB, Stolitchnov I, Taganstev AK, Taylor DV, Yamada T, Streiffer S (2006) J Appl Phys 100:051606
5. Auciello O, Scott JF, Ramesh R (1998) Phys Today 51:22
6. Vrejoiu I, Le Rhun G, Pintilie L, Hesse D, Alexe M, Gösele U (2006) Adv Mater 18:1657
7. Rodriguez Contreras J, Petraru A, Kohlstedt H, Schubert J, Poppe U, Buchal Ch, Waser R (2005) J Cryst Growth 277:210
8. Okikawa T, Morioka H, Nagai A, Funakubo H (2004) Appl Phys Lett 85:1754
9. Asano G, Okikawa T, Funakobo H (2003) Jpn J Appl Phys 42:2801
10. Kato Y, Kaneko Y, Tanaka H, Kaibara K, Koyama S, Isogai K, Yamada T, Shimada Y (2007) Jpn J Appl Phys 46:2157
11. Schwartz RW, Schneller T, Waser R (2004) C R Chim 7:433
12. Dobberstein H, Schwartz RW (2002) Proc 1st Symp Adv Met Next Generation, Prelude to Func-Int Mat. ASIT Chubu, Nagoya, Japan
13. Bolten D, Böttger U, Schneller T, Grossmann M, Lohse O, Waser R (2000) Appl Phys Lett 77:3830
14. Klissurska RD, Brooks KG, Reaney IM, Pawlaczyk C, Kosec M, Setter N (1995) J Am Ceram Soc 78:1513
15. Chang J-F, Desu SB (1994) J Mater Res 9:955
16. Schwartz RW, Boyle TJ, Lockwood SJ, Sinclair MB, Dimos D, Buchheit CD (1995) Integr Ferroelectr 7:259
17. Kwok CK, Desu SB (1993) J Mater Res 8:339
18. Kim S-H, Park D-Y, Woo H-J, Lee D-S, Ha J, Hwang CS, Shim I-B, Kingon AI (2002) Thin Solid Films 416:264
19. Huang Z, Zhang Q, Whatmore RW (1998) J Mater Sci Lett 17:1157
20. Chen S-Y, Chen I-W (1994) J Am Ceram Soc 77:2332
21. Kaewchinda D, Chairaungsri T, Naksata M, Milne SJ, Brydson R (2000) J Eur Ceram Soc 20:1277
22. Schneller T, Waser R (2007) J Sol-Gel Sci Technol 42:337
23. Norga GJ, Fe L (2001) Mater Res Soc Symp Proc 655:CC9.1.1
24. Ellerkmann U, Schneller T, Nauenheim C, Böttger U, Waser R (2008) Thin Solid Films 516:4713
25. Kohlstedt H, Mustafa Y, Gerber A, Petraru A, Fitsilis M, Meyer R, Böttger U, Waser R (2005) Microelectron Eng 80:296
26. Assink RA, Schwartz RW (1993) Chem Mater 5:511
27. Nouwen R, Mullens J, Franco D, Yperman J, Van Poucke LC (1996) Vib Spectrosc 10:291
28. Cao D, Jeong I-K, Heffner RH, Darling T, Lee JK, Bridges F, Park J-S, Hong K-S (2004) Phys Rev B 70:224102
29. Bertagnolli H, Ertel TS (1994) Angew Chem Int Ed Engl 33:45
30. Malič B, Arčon I, Kodre A, Kosec M (2006) J Appl Phys 100:051612
31. Malič B, Kosec M, Arčon I, Kodre A (2005) J Eur Ceram Soc 25:2241
32. Malič B, Arčon I, Kosec M, Kodre A (1997) J Mater Res 12:2602
33. Sengupta SS, Ma L, Adler DL, Payne DA (1995) J Mater Res 10:1345
34. Cao D, Jeong L-K, Heffner RH, Darling T, Lee J-K (2004) Phys Rev B 70:224102
35. Carlislie JA, Blankenship SR, Smith RN, Shirley EL, Terminello LJ, Jia JJ, Callcott TA, Ederer DL (1999) J Electr Spectrosc Relat Phenom 101:839
36. Eisebitt S, Lüning J, Rubensson J-E, Eberhardt W (1999) Phys Stat Sol (b) 215:803
37. Guo J (2004) Int J Nanotechnol 1:193
38. de Groot FMF, Grioni M, Fuggle JC, Ghijsen J, Sawatzky GA, Petersen H (1989) Phys Rev B 40:5715
39. Nordgen J, Guo J (2000) J Electr Spectrosc Relat Phenom 110–111:1
40. Kotani A, Shin S (2001) Rev Mod Phys 73:203
41. Guo J, Skytt P, Wassdahl N, Nordgren J (2000) J Electr Spectrosc Relat Phenom 110:41
42. Shirley EL (1997) Phys Rev Lett 80:797
43. Finkelstein LD, Kurmaev EZ, Korotin MA, Moewes A, Schneider B, Butorin SM, Guo J-H, Nordgren J, Hartmann D, Neumann M, Ederer DL (1999) Phys Rev B 60:2212
44. Butorin SM, Guo J-H, Magnuson M, Nordgren J (1997) Phys Rev B 55:4242
45. Schneller T, Menzel S, Waser R, manuscript in preparation
46. Jia JJ, Callcott TA, Yurkas J, Ellis AW, Himpsel FJ, Samant MG, Stöhr J, Ederer DL, Carlisle JA, Hudson EA, Terminello LJ, Shuh DK, Perera RCC (1995) Rev Sci Instrum 66:1394
47. Gong W, Li J-F, Chu X, Li L (2004) J Eur Ceram Soc 24:2977
48. Fè L, Norga GJ, Wouters DJ, Maes HE, Maes G (2001) J Mater Res 16:2499
49. Brooks KG, Reaney IM, Klissurska R, Huang Y, Bursill L, Setter N (1994) J Mater Res 9:2540
50. Soriano L, Abbate M, Fernández A, González-Elipe AR, Sanz JM (1997) Surf Interface Anal 25:804
51. de Groot FMF, Fuggle JC, Thole BT, Sawatzky GA (1990) Phys Rev B 41:928
52. de Groot FMF, de Groot FM, Faber J, Michiels JJ, Czyżyk MT, Abbate M, Fuggle JC (1993) Phys Rev B 48:2074
53. Ruus R, Kikas A, Saar A, Ausmees A, Nömmiste E, Aarik J, Aidla A, Uustared T, Martinson L (1997) Solid State Comm 104:199
54. Kucheyev SO, Baumann TF, Wang YM, van Buuren T, Satcher JH Jr (2005) J Electr Spectrosc Relat Phenom 144:609

55. Augustsson A, Henningsson A, Butorin SM, Siegbahn H, Nordgren J, Guo JH (2003) J Chem Phys 119:3983
56. Harada Y, Kinugasa TT, Eguchi R, Matsubara M, Kotani A, Watanabe M, Yagishita A, Shin S (2000) Phys Rev B 61:12854
57. Cromcombette JP, Jollet F (1994) J Phys Condens Matter 6:10811
58. Ranade MR et al (2002) Proc Natl Acad Sci 99:6476
59. Lussier A, Dvorak J, Idzerda YU, Shinde SR, Oagle SB, Venkatesan T (2005) Phys Scr T115:623
60. Watanabe A, Tsuchiya T, Imai Y (2002) Thin Solid Films 406:132
61. Muralt P, Maeder T, Sagalowicz L, Hiboux S, Scalese S, Naumovic D, Agostino RG, Xanthopoulos N, Mathieu HJ, Patthey L, Bullock EL (1998) J Appl Phys 83:3835
62. Finkelstein LD, Kurmaev EZ, Korotin MA, Moewes A, Schneider B, Butorin SM, Guo J-H, Nordgren J, Hartmann D, Neumann M, Ederer DL (1999) Phys Rev B 60:2212
63. Butorin SM, Guo J-H, Magnuson M, Kuiper P, Nordgren J (1996) Phys Rev B 54:4405
64. Butorin SM (2000) J Electr Spectrosc Relat Phenom 110–111:213
65. Higuchi T, Tsukamoto T, Hattori T, Honda Y, Yokoyama S, Funakubo H (2005) Jpn J Appl Phys 44:6923
66. Cohen RE, Krakauer H (1990) Phys Rev B 42:6416
67. Higuchi T, Tsukamoto T, Oka K, Yokoya T, Tezuka Y, Shin S (1999) Jpn J Appl Phys 38:5667
68. Higuchi T, Tsukamoto T, Sata N, Ishigame M, Tezuka Y, Shin S (1998) Phys Rev B 57:6978
69. Miyazawa H, Natori E, Miyashita S, Shimoda T, Ishii F, Oguchi T (2000) Jpn J Appl Phys 39:5679
70. Hamilton TD (2005) PhD thesis, Determinig the sp^2/sp^3 bonding concentration of carbon films. University of Saskatchewan
71. Sham TK, Yang BX, Kirz J, Tse JS (1989) Phys Rev B 40:6532
72. Tani T, Xu Z, Payne DA (1993) Mater Res Soc Symp Proc 310:269
73. Song YJ, Zhu Y, Desu SB (1998) Appl Phys Lett 72:2686
74. Al-Shareef HN, Gifford KD, Rou SH, Hren PD, Auciello O, Kingon A (1993) Integr Ferroelectr 3:321
75. Reaney IM, Brooks K, Klissurska R, Pawlacyk C, Setter N (1994) J Am Ceram Soc 77:1209
76. Liu Y, Phulé P-P (1996) J Am Ceram Soc 79:495
77. Spierings GACM, Ulenaers MJE, Kampschöer GLM, van Hal HAM, Larsen PK (1991) J Appl Phys 70:2290
78. Zhao JS, Sim JS, Lee HJ, Park D-Y, Hwang GW, Lee K, Hwang CS (2006) J Electrochem Soc 153:F81
79. Chen S-Y, Chen I-W (1994) J Am Ceram Soc 77:2337
80. Chen S-Y, Chen I-W (1998) J Am Ceram Soc 81:97
81. Tani T, Xu Z, Payne DA (1993) Mater Res Soc Symp Proc 310:269
82. Gong W, Li J-F, Chu X, Gui Z, Li L (2004) Acta Mater 52:2787
83. Kalpat S, Uchino K (2001) J Appl Phys 90:2703
84. Chen SY (1996) Mater Chem Phys 45:159